Published in final edited form as:
Nanoscale. 2017 May 18; 9(19): 6463–6470. doi:10.1039/c7nr01148b.

Core@shell, Au@TiO_x nanoparticles by gas phase Synthesis

L. Martínez[a], **A. Mayoral**[b], **M. Espiñeira**[a], **E. Roman**[a], **F. J. Palomares**[a], and **Y. Huttel**[*,a]

[a]Instituto de Ciencia de Materiales de Madrid, Consejo Superior de Investigaciones Científicas (CSIC), C/Sor Juana Inés de la Cruz, 3, 28049 Madrid, Spain

[b]Laboratorio de Microscopías Avanzadas (LMA), Instituto de Nanociencia de Aragón (INA), Universidad de Zaragoza, c/Mariano Esquillor, Edificio I+D, 50018 Zaragoza, Spain

Abstract

Herein, gas phase synthesis and characterization of multifunctional core@shell, Au@TiO_x nanoparticles have been reported. The nanoparticles were produced via a one-step process using a multiple-ion cluster source under a controlled environment that guaranteed the purity of the nanoparticles. The growth of the Au cores (6 nm diameter) is stopped when they pass through the Ti plasma where they are covered by an ultra-thin (1 nm thick) and homogeneous titanium shell that is oxidized in-flight before the soft-landing of the nanoparticles. The Au cores were found to be highly crystalline with icosahedral (44%) and decahedral (66%) structures, whereas the shell, mainly composed of TiO_2 (79%), was not ordered. The highly electrical insulating behaviour of the titanium oxide shell was confirmed by the charging effect produced during X-ray photoemission spectroscopy.

Introduction

The research area of core@shell nanoparticles (NPs) has received significant interest in the last decade.1 The different elemental composition and interactions of the core and shell allow the tailored fabrication of NPs with chemical and physical responses that can be controlled through external stimuli.2 This implied that properties, such as electrical charge, functionality, reactivity of the surface, and stability of the NPs, which could not be tuned in the past, can now be tuned.3 These properties have invoked the importance of core@shell NPs in various fields such as biomedicine,4,5 energy,6–8 electronics,9,10 optics,11 and catalysis,12–15 and these core@shell NPs offer better responses in comparison to single element NPs.

Moreover, adding a shell to a NP modifies the core-distance interaction of the interparticles, which directly depends on the thickness of the shell. Furthermore, the shell can protect the core from chemical reactions with the environment and impurities inherently generated during the fabrication processes.16,17 All these properties make core–shell NPs very attractive not only for fundamental studies at nanoscale but also for various applications as abovementioned. One of the applications is catalysis that has attracted significant attention. For example, Au@TiO_x NPs have been proven to be catalytically active for CO oxidation

huttel@icmm.csic.es.

Europe PMC Funders Author Manuscripts

process18,19 and photoactive at nanoscale: Au becomes a light absorber because of the surface plasmon resonance (SPR), whereas titania becomes photocatalytic.20–22 These interesting properties originate due to the interaction between Au (conductor) and TiO_2 (big band gap semiconductor) as well as due to SPR-mediated electron transfer from the Au core to the TiO_2 shell when the NPs are illuminated by visible light.23,24 In both cases, NPs response can be tuned by modifying the radius of the core and the thickness of the shell.25

The purity of core@shell NPs is crucial for most of the applications.17 Nowadays, chemical precipitation and hydrolysis16–18,20,26 are widely used fabrication techniques due to their lower cost and mass production capacities. However, these techniques are intrinsically limited when high compositional purity of NPs,27–32 narrow size distribution,33–35 and absence of agglomerates are required.36–38 To the best of our knowledge, Au@TiO_2 nanoparticles were previously synthesized via chemical methods;16,20 but with the abovementioned intrinsic limitations.

Alternatively, gas phase synthesis of nanoparticles can be used to produce a wide variety of nanoparticles under controlled environment, thereby warranting the purity of the fabricated nanoparticles. The gas phase synthesis has been used over 3 decades for the growth of different NPs.39–55 More detailed information about gas phase synthesis of nanoparticles and cluster sources can be found elsewhere.56–61

Briefly, the gas phase synthesis of NPs is performed by the evaporation of a given material (by thermal evaporation, sublimation, sputtering, laser ablation, etc.) under vacuum conditions (which prevent contamination) and the subsequent aggregation of atoms/ions to form clusters (<100 atoms) or nanoparticles (>100 atoms). Note that the definition of cluster is not unique. Another definition assumes that clusters are those entities that have a diameter below 1 nm, whereas for diameters between 1 nm and 100 nm, the terminology of nanoparticle was preferred. Due to the advantages of providing a good control over the mean size and size distribution as well as high purity of the generated NPs, the gas phase synthesis has become a very attractive synthesis method for fundamental nanoscience studies and nanotechnology. Since the seminal work of H. Haberland and co-workers,62,63 ion cluster sources (ICS) based on magnetron sputtering have gained popularity. The ability to control the deposition rate of NPs and hence the coverage of NPs allows the deposition of NPs that are not agglomerated. NPs grown using ICS have been the subject of fundamental64–71 and applied studies.72–74 Furthermore, combination of ICS with additional evaporators allows the formation of core@shell nanoparticles such as Fe@Cr, Ag@MgO, and Pt@TiO_2 that have been used for fundamental75–77 and applied studies in energy and catalysis.78,79

The recent advent of a new generation of cluster sources were the single magnetron is replaced by more than one magnetron, and hence by more than one target material, has opened a route for the fabrication of more sophisticated nanoparticles80–88 and even of novel bimetallic core@shell nanoparticles.89

In the present study, catalysis was not considered. Herein, the use of two independent magnetrons into an aggregation source that allowed the formation of well-defined Au@TiO_x nanoparticles with high control over chemical composition, mean diameter, and size

distribution has been reported for the first time. The morphology, atomic and electronic structures of the synthesized Au@TiO_x nanoparticles have also been reported.

Experimental

The nanoparticles (NPs) were grown using the multiple ion cluster source (MICS), which is an adaptation of the standard ion cluster source (ICS). In MICS, the single magnetron is replaced by 3 independent magnetrons.80 This modification has been shown to be very effective for the fabrication of nanoparticles with tuneable chemical composition and complex structures such as core@shell or even core@shell@shell; moreover, this strategy provides control over the size and size distribution of the NPs. Fig. 1 displays a schematic of the MICS (top of Fig. 1), where 2 of the 3 magnetrons are presented (M1 and M2) inside the aggregation zone (AZ). The magnetrons have individual translation systems that allow the individual positioning of the magnetrons heads and hence of the corresponding plasmas. As shown in Fig. 1, M1 is placed behind M2. The MICS is an Ultra High Vacuum (UHV) system (base pressure $5 \times 10_{-10}$ mbar) that is differentially pumped by a turbomolecular pump attached to a flange (cf. DP in Fig. 1(a)) and also through an exit slit where the NPs are extracted (cf. exit in Fig. 1(a)) before they are collected on appropriate substrates located in an UHV deposition chamber placed after the exit slit. Fig. 1(b) illustrates the formation of NPs from the material placed in magnetron 1. In the present study, magnetron 1 was loaded with a pure gold target (99.99% purity). The ions extracted by sputtering agglomerate and form the Au NPs that exit the aggregation zone. The same process has been illustrated for magnetron 2 (cf. Fig. 1(c)) that was loaded with a pure Ti target (99.99% purity). In both cases, the path of the ions exiting the aggregation zone was long enough for the formation of the nanoparticles. The working parameters, deposition rates, and coverages have been tabulated in Table 1 of the ESI.† Taking advantage of the individual positioning of the magnetrons, it was possible to form a Au nanoparticle first that was further coated by Ti, as depicted in Fig. 1(d). In this case, the growth of the Au NPs was stopped when Au NPs travelled through the Ti ion plasma, which induced the formation of a Ti shell. Following the procedure of S. D'Addato et al.,90,91 Ti NPs were oxidized in-flight before their landing on the substrates by the controlled injection of pure oxygen (through a leak valve) into the deposition chamber attached to the MICS (oxygen base pressure of $5 \times 10_{-5}$ mbar). Due to high oxygen affinity of titanium atoms, they reacted in flight with oxygen, forming a titanium oxide shell before the landing of the nanoparticles. Note that oxygen was not directly injected into the MICS such that to avoid poisoning of the Ti sputtering through the formation of an insulating Ti oxide layer on the target itself. In the present study no mass filtering was applied due to the inherent narrow size distribution; neutral, cationic and anionic species were allowed to be deposited on different substrates.

The NPs were deposited on flat Si(100) polished wafers (roughness below 1 nm) and amorphous carbon-coated TEM grids, placed at the exit of the MICS for the characterization of NPs via atomic force microscopy (AFM), transmission electron microscopy (TEM) and X-ray photoemission spectroscopy (XPS). To avoid charging effects during NPs deposition and XPS measurements, p-doped (boron) Si(100) wafers were used (1.0–10.0 ohm cm).

Europe PMC Funders Author Manuscripts

AFM measurements were carried out using Cervantes AFM System from Nanotec Electronica S.L. The samples were measured in the dynamic mode using tips from Next-Tip S.L.92,93 and the images were obtained using the WSxM software.94 TEM measurements were performed using an FEI-TITAN X-FEG transmission electron microscope in the STEM mode, operated at 300 kV and 120 kV. The images were acquired using a high angle annular dark field (HAADF) detector. The microscope was equipped with a monochromator, Gatan Energy Filter Tridiem 866 ERS, a spherical aberration corrector (CEOS) for the electron probe, allowing an effective 0.08 nm spatial resolution, and an energy dispersive X-ray detector for EDS analysis.

XPS was used to characterize the chemical composition and electronic states of the NPs deposited on Si wafer substrates. XPS spectra were acquired in a separate UHV chamber, with the base pressure of 10_{-10} mbar, equipped with a hemispherical electron energy analyzer (SPECS Phoibos 150 spectrometer) and a delay-line detector using a monochromatic AlKα (1486.74 eV) X-ray source.95,96 Spectra were obtained at normal emission take-off angle using an energy step of 0.025 eV and a pass-energy of 20 eV, which provided an overall instrumental peak broadening of 0.5 eV. The absolute binding energies of the photoelectron spectra were determined by referencing to the Si $2p_{3/2}$ transition at 99.0 eV. Data processing was performed using the CasaXPS software (Casa software Ltd, Cheshire, UK).

Results and discussion

Morphology and structure of the nanoparticles

All the deposits were characterized by AFM in terms of the NP size (measured height), size distribution, and deposition rates. Representative AFM images of Au, TiO_x, and Au@TiO_x NPs are presented in Fig. 2(a), (b), and (c), respectively.

The flat Si wafer substrates were suitable for the precise determination of the NPs height. The statistical study of each deposit resulted in a mean size and a standard deviation of 5.5 ± 0.8 nm, 6.5 ± 0.8 nm, and 6.5 ± 0.8 nm for Au, TiO_x, and Au@TiO_x NPs, respectively. For each deposit, the height of around 100 NPs was individually obtained. Although AFM is very precise for the determination of the height of the NPs, intrinsic convolution of the tip shape with the NPs does not allow the correct determination of the diameter of the NPs. On the other hand, the TEM approach is a very precise tool for the determination of the diameters, internal structural order, and chemical composition of the NPs. All the deposits were characterized via TEM. Fig. 3 displays the representative spherical aberration (Cs-corrected) STEM-HAADF images of the Au NPs. Both icosahedral (Ih) and decahedral (Dh) crystalline orders were identified in Au NPs. To acquire the images with minimum interaction between the electron beam and the NPs (cf. Fig. S1 of the ESI†), the experimental conditions were set as follows: beam convergence semi-angle was 17.5 mrad and the inner angle of the detector was 90 mrad and the outer angle was 200 mrad. The pixel time was typically 8 μs per pixel with the current of 15 pA. Although rotation of the nanoparticles was observed under electron beam, no significant structural changes were observed under these conditions. To provide a clear image of the homogeneity of the material produced, images at different magnification were obtained (cf. Fig. S2 of the ESI†).

Fig. 3(a) shows the Cs-corrected STEM-HAADF image of an Ih Au nanoparticle sitting on the two-fold axis and its corresponding fast Fourier transform (FFT) pattern (inset); Fig. 3(b) corresponds to a representative Dh Au NP along its five-fold axis, where the 5 tetrahedra linked through twinned planes can be clearly identified, and FFT has also been shown (inset). The statistical study performed on 85 NPs revealed that both structures were present in similar amounts and showed similar diameters of 4.55 ± 0.46 nm (44%) and 5.28 ± 0.69 nm (66%) for Ih and Dh structures, respectively. These diameters correspond to the mean height determined by AFM within the experimental uncertainty, which confirms the soft-landing of the NPs.97

While pure Au NPs displayed high crystalline order, pure TiO_x NPs were found to be mainly amorphous. Only a few fractions of TiO_x nanoparticles displayed some crystalline order. Fig. 4(a) shows a representative Cs-corrected STEM image of the TiO_x NP. The statistical mean diameter of the NPs was 6.52 ± 0.42 nm (statistics performed on 132 NPs). With the intention to corroborate the chemical nature of the TiO_x NPs, electron energy loss spectroscopy (EELS) analyses were performed. Fig. 4(b) and (c) display the spectral images (51 × 43 pixels, 0.15 s per pixel) extracted from Ti-$L_{2,3}$ and O-K edges, clearly showing that both Ti and O were distributed in the entire nanoparticle, thereby confirming that the Ti NPs were fully oxidized (cf. EELS spectrum in Fig. S3 of the ESI†).

Moreover, the STEM characterization of the Au@TiO_x nanoparticles was also conducted. The electron microscopy observations revealed that all NPs had Au@TiO_x structure and neither pure Au nor TiO_x nanoparticles were deposited. As can be seen in Fig. 5, by the observation of different contrast in the image, TiO_x shell can be clearly identified (for lower magnification images, cf. Fig. S4 in the ESI†). Moreover, chemical analyses (both EDS and EELS) were performed to confirm this assumption (cf. EDS and EELS spectra in Fig. S5 and S6, respectively, of the ESI†). For the Au@TiO_x nanoparticles, the statistics obtained over 132 particles resulted in 44% Ih Au core of 6.43 ± 0.39 nm diameter and 66% Dh Au core of 6.90 ± 0.61 nm diameter; moreover, a TiO_x shell thickness of about 1 nm was observed in all the cases. Fig. 5(a) displays a Au icosahedron orientated along the five-fold symmetry axis, with a thin overlayer (about 1 mm thick) of a disordered material. The chemical EDS analysis was carried out along the white arrow plotted in Fig. 5(a); the results are displayed in Fig. 5(b) where the chemical composition of the NPs can be observed. It clearly appeared that a Ti shell (blue line) coated the Au core of 5–6 nm diameter (orange line).

Based on the direct observation of Fig. 5(a), it was concluded that Au formed the core of the nanoparticles due to the heavy nature of Au as compared to that of Ti and O;98 moreover, the spectral image analysis carried out on a representative nanoparticle confirmed the Au@TiO_x structure, as represented in Fig. 5(c). The Cs-corrected STEM-HAAF chemical mapping was performed by obtaining the Ti-$L_{2,3}$ signal (blue color) and the Au-$M_{5,4}$ signal (orange color).

Electronic structure of the nanoparticles

Fig. 6 shows the Ti 2p core level spectra for TiO_x and Au@TiO_x NPs. The spectra have been fitted with the minimum number of components, compatible with the expected chemistry.

For peak fitting, a Gaussian and Lorentzian product was used. The Lorentzian contribution was 30% and 60% for TiO_x and Au@TiO_x NPs, respectively. The fitting was performed on both the Ti $2p_{1/2}$ and Ti $2p_{3/2}$ spin–orbit peaks to warrant the coherence of the procedure and assume a Shirley background model. The Ti 2p core level spectra displayed a complex structure with shakeup features at higher binding energy side in both transitions. For simplicity, only the Ti $2p_{3/2}$ emission has been discussed. In both cases (TiO_x and Au@TiO_x NPs), peaks located at 458.8 eV and 457.4 eV reveal the presence of Ti_{4+} and Ti_{3+}, respectively, although the latter component is much more intense in the case of Au@TiO_x NPs. In both cases, the main component corresponds to Ti_{4+}. The percentages of Ti_2O_3 are 21 (±12)% and 8 (±6)% for Au@TiO_x and TiO_x NPs, respectively, whereas for TiO_2, they are 79 (±12)% and 92 (±6)%, respectively. The higher contributions of Ti_{3+} for the case of Au@TiO_x NPs could indicate a stronger catalytic reactivity.99

The corresponding Au 4f core level photoemission spectra were obtained and are presented in Fig. 7; a reference Au 4f spectrum corresponding to Au NPs of the same size but grown without the injection of oxygen in the deposition chamber is also presented for comparison. Again, the spectra of both spin–orbit components are shown but only the results of Au $4f_{7/2}$ have been discussed for simplicity. While in Au, Au $4f_{7/2}$ bulk and surface components were referenced at 84.0 and 83.5 eV, respectively, previous works have reported that these binding energy values in the case of nanoparticles can be different depending on the synthesis method, density of NPs or interactions with the environment (substrate, exposure to air, etc.). 100–103 In fact, in a recent review published by Villa et al., it was reported that Au0 binding energies in Au NPs were in the range from 84.5 to 82.9 eV,104 confirming the lack of consensus. Herein, we focussed on the possible differences in the binding energy values of Au 4f levels in pure Au NPs with NPs grown in the presence of oxygen and Au@TiO_x NPs. Fig. 7 clearly shows that the spectra for Au NPs grown with and without injecting oxygen are very similar. This demonstrated that the injection of oxygen in the deposition chamber for the in-flight oxidation of the titanium shell did not substantially affect the growth of the Au NPs cores. The main peak appeared at the binding energy of 83.5 eV. A second peak located at 84.4 eV could correspond to the presence of Au1+.105 In the case of Au@TiO_x NPs, the fitting procedure resulted in the identification of two peaks like in the case of Au NPs, but shifted to higher binding energy by about 0.3 eV. This shift in the binding energy indicated that the Au cores were positively charged, which was consistent with the electron photoemission current that escaped from the Au cores and could not be fully compensated (the samples were ground in the XPS setup) due to the strong insulating behaviour of the TiO_x shell.

Conclusions

Au, TiO_x, and Au@TiO_x nanoparticles were synthesized in the gas phase via the multi-magnetron approach. The synthesis was performed in one-step, and the titanium shell was oxidized in flight before the soft-landing of the nanoparticles. The morphological, atomic and electronic structure characterizations of the nanoparticles were performed. In particular, it was shown that Au@TiO_x nanoparticles were made of a 6 nm diameter highly crystalline Au core homogeneously covered by a 1 nm thick amorphous TiO_x shell. It was found that

the titanium oxide shell was mainly composed of TiO_2 (Ti_{4+}) that strongly insulated the Au metallic core.

Acknowledgements

This work was supported by the European ERC-2013-SyG 610256 NANOCOSMOS and European Union Seventh Framework Programme under grant agreement no. 604391 FET Graphene Flagship and by the Spanish Ministerio de Ciencia e Innovación under projects no. MAT2014-59772-C2-2-P and MAT2016-80394-R. A. M. acknowledges the Government of Aragon and the European Social Fund under the project grant number E/26 “Construyendo Europa desde Aragón” 2014–2020.

Notes and references

1. Ghosh Chaudhuri R, Paria S. Chem Rev. 2012; 112:2373–2433. [PubMed: 22204603]
2. Caruso F. Adv Mater. 2001; 13:11–22.
3. Gawande MB, Goswami A, Asefa T, Guo H, Biradar AV, Peng DL, Zboril R, Varma RS. Chem Soc Rev. 2015; 44:7540–7590. [PubMed: 26288197]
4. Chatterjee K, Sarkar S, Jagajjanani Rao K, Paria S. Adv Colloid Interface Sci. 2014; 209:8–39. [PubMed: 24491963]
5. Laurent S, Forge D, Port M, Roch A, Robic C, Vander Elst L, Muller R. Chem Rev. 2008; 108:2064–2110. [PubMed: 18543879]
6. Guchhait A, Rath AK, Pal AJ. Chem Mater. 2009; 21:5292–5299.
7. Zheng DJ, Pang XC, Wang MY, He YJ, Lin CJ, Lin ZQ. Chem Mater. 2015; 27:5271–5278.
8. Cui E, Lu G. Int J Hydrogen Energy. 2014; 39:8959–8968.
9. Malaikal A, Katz H, Cotts P, Subramoney S, Mirau P. J Am Chem Soc. 2005; 127:14655–14662. [PubMed: 16231918]
10. Kim CK, Lee G-J, Lee MK, Rhee CK. Powder Technol. 2014; 263:1–6.
11. Wang L, Clavero C, Huba Z, Carroll KJ, Carpenter EE, Gu D, Lukaszew RA. Nano Lett. 2011; 11:1237–1240. [PubMed: 21319843]
12. Lin J-H, Guliants VV. Appl Catal A. 2012:445–446. 187-194.
13. Wang D, Zhao P, Li Y. Sci Rep. 2011; 1:37. [PubMed: 22355556]
14. Chen D, Li C, Liu H, Ye F, Yang J. Sci Rep. 2015; 5:11949. [PubMed: 26144550]
15. Froemming NS, Henkelman G. J Chem Phys. 2009; 131:234103. [PubMed: 20025310]
16. Anandan S, Ashokkumar M. Ultrason Sonochem. 2009; 16:316–320. [PubMed: 19028129]
17. Yu Y, Mulvaney P. Mater Trans. 2004; 45:964–967.
18. Overbury S, Schwartz V, Mullins D, Yan W, Dai S. J Catal. 2006; 241:56–65.
19. Schwartz V, Mullins D, Yan D, Chen B, Dai S, Overbury S. J Phys Chem Chem B. 2004; 108:15782–15790.
20. Kanda T, Komata K, Torigoe K, Endo T, Sakai K, Abe M, Sakai H. J Oleo Sci. 2014; 63:507–513. [PubMed: 24717542]
21. Miljevic M, Geiseler B, Bergfeldt T, Bockstaller P, Fruk L. Adv Funct Mater. 2014; 24:907–915.
22. Dollinger A, Stolch L, Luo Y, Beck M, Strobel CH, Hagner M, Dilger S, Bein M, Polarz S, Gantefoer GF, Kim YD, et al. Phys Chem Chem Phys. 2014; 16:11017–11023. [PubMed: 24777154]
23. Hou W, Cronin SB. Adv Funct Mater. 2013; 23:1612–1619.
24. Eustis S, el-Sayed MA. Chem Soc Rev. 2006; 35:209–217. [PubMed: 16505915]
25. Kwon H, Lim Y, Tripathy S, Kim B, Lee M, Yu YT. Jpn J Appl Phys. 2007; 47:2567–2570.
26. Wu XF, Song HY, Yoon JM, Yu YT, Chen YF. Langmuir. 2009; 25:6438–6447. [PubMed: 19341284]
27. Mansfield E, Tyner KM, Poling CM, Blacklock JL. Anal Chem. 2014; 86:1478–1484. [PubMed: 24400715]

28. Russo R, Cianchi A, Akhmadeev YH, Catani L, Langner J, Lorkiewicz J, Polini R, Ruggiero B, Sadowski MJ, Tazzari S, Koval NN. Surf Coat Technol. 2006; 201:3987–3992.
29. Nel AE, Madler L, Velegol D, Xia T, Hoek EM, Somasundaran P, Klaessig F, Castranova V, Thompson M. Nat Mater. 2009; 8:543–557. [PubMed: 19525947]
30. Zhang B, Yan B. Anal Bioanal Chem. 2010; 396:973–982. [PubMed: 19644676]
31. Kamaly N, Xiao Z, Valencia PM, Radovic-Moreno AF, Farokhzad OC. Chem Soc Rev. 2012; 41:2971–3010. [PubMed: 22388185]
32. Fenaroli F, Westmoreland D, Benjaminsen J, Kolstad T, Skjeldal FM, Meijer A, van der Vaart M, Ulanova L, Roos N, Nyström B, Hildhal J, et al. ACS Nano. 2014; 8:7014–7026. [PubMed: 24945994]
33. Chan A, Lewis J. Langmuir. 2008; 24:11399–11405. [PubMed: 18816017]
34. Deeb C, Zhou X, Plain J, Wiederrecht GP, Bachelot R, Russell M, Jain PK. The J Phys Chem C. 2013; 117:10669–10676.
35. Devadoss A, Dickinson C, Keyes TE, Forster RJ. Anal Chem. 2011; 83:2383–2387. [PubMed: 21361366]
36. Liu HH, Surawanvijit S, Rallo R, Orkoulas G, Cohen Y. Environ Sci Technol. 2011; 45:9284–9292. [PubMed: 21916459]
37. de Martin L, Bouwman WG, van Ommen JR. Langmuir. 2014; 30:12696–12702. [PubMed: 25313446]
38. Zook J, Rastogi V, MacCuspie R, Keene A, Fagan J. ACS Nano. 2011; 5:8070–8079. [PubMed: 21888410]
39. Baker SH, Thornton SC, Keen AM, Preston TI, Norris C, Edmonds KW, Binns C. Rev Sci Instrum. 1997; 68:1853–1857.
40. Iles GN, Baker SH, Thornton SC, Binns C. J Appl Phys. 2009; 105:024306.
41. Eberhardt W. Surf Sci. 2002; 500:242–270.
42. Lau JT, Achleitner A, Ehrke HU, Langenbuch U, Reif M, Wurth W. Rev Sci Instrum. 2005; 76:063902.
43. Di Vece M, Bals S, Verbeeck J, Lievens P, Van Tendeloo G. Phys Rev B: Condens Matter. 2009; 80:125420.
44. Maicas M, Sanz M, Cui H, Aroca C, Sánchez P. J Magn Magn Mater. 2010; 322:3485–3489.
45. Pohl D, Surrey A, Schultz L, Rellinghaus B. Appl Phys Lett. 2012; 101:263105.
46. Ruano M, Diaz M, Martinez L, Navarro E, Roman E, Garcia-Hernandez M, Espinosa A, Ballesteros C, Fermento R, Huttel Y. Phys Chem Chem Phys. 2013; 15:316–329. [PubMed: 23165521]
47. Llamosa Pérez D, Espinosa A, Martínez L, Román E, Ballesteros C, Mayoral A, García-Hernández M, Huttel Y. J Phys Chem C. 2013; 117:3101–3108.
48. Drache S, Stranak V, Hubicka Z, Berg F, Tichy M, Helm CA, Hippler R. J Appl Phys. 2014; 116:143303.
49. Manchanda P, Kumar P, Balasubramanian B, Mukherjee P, Kashyap A, Sellmyer DJ, Skomski R. IEEE Trans Magn. 2014; 50:1–4.
50. Lopez Anton R, Gonzalez JA, Andres JP, Canales- Vazquez J, De Toro JA, Riveiro JM. Nanotechnology. 2014; 25:105702. [PubMed: 24532090]
51. Palmer RE, Cao L, Yin F. Rev Sci Instrum. 2016; 87:046103. [PubMed: 27131719]
52. Oprea B, Martinez L, Roman E, Vanea E, Simon S, Huttel Y. Langmuir. 2015; 31:13813–13820. [PubMed: 26640032]
53. Balcells L, Martinez-Boubeta C, Cisneros-Fernandez J, Simeonidis K, Bozzo B, Oro-Sole J, Bagues N, Arbiol J, Mestres N, Martinez B. ACS Appl Mater Interfaces. 2016; 8:28599–28606.
54. Gunnarsson R, Pilch I, Boyd RD, Brenning N, Helmersson U. J Appl Phys. 2016; 120:044308.
55. Jimenez-Villacorta F, Climent-Pascual E, Ramirez-Jimenez R, Sanchez-Marcos J, Prieto C, de Andrés A. Carbon. 2016; 101:305–314.
56. Xirouchaki C, Palmer RE. Philos Trans R Soc A. 2004; 362:117–124.

57. Bansmann J, Baker S, Binns C, Blackman J, Bucher J, Dorantesdavila J, Dupuis V, Favre L, Kechrakos D, Kleibert A. Surf Sci Rep. 2005; 56:189–275.
58. Wegner K, Piseri P, Tafreshi HV, Milani P. J Phys D: Appl Phys. 2006; 39:R439–R459.
59. Binns C, Trohidou KN, Bansmann J, Baker SH, Blackman JA, Bucher JP, Kechrakos D, Kleibert A, Louch S, Meiwes-Broer KH, Pastor GM, et al. J Phys D: Appl Phys. 2005; 38:R357–R379.
60. Perez A, Melinon V, Dupuis V, Bardotti L, Masenelli B, Tournus F, Prével B, Tuaillon-Combes J, Bernstein E, Tamion A, Blanc N, et al. Int J Nanotechnol. 2010; 7:523.
61. Huttel, Y. Gas-Phase Synthesis of Nanoparticles. Wiley; 2017.
62. Haberland H, Karrais M, Mall M. Z Phys D: At Mol Clusters. 1991; 20(1-4):413–415.
63. Haberland H, Karrais M, Mall M, Thurner Y. J Vac Sci Technol A. 1992; 10:3266–3271.
64. Shyjumon I, Gopinadhan M, Helm CA, Smirnov BM, Hippler R. Thin Solid Films. 2006; 500:41–51.
65. Mayoral A, Mejia-Rosales S, Mariscal MM, Perez-Tijerina E, Jose-Yacaman M. Nanoscale. 2010; 2:2647–2651. [PubMed: 20944844]
66. Rosellen W, Kleinhans C, Hückelkamp V, Bulut F, Kleibert A, Bansmann J, Getzlaff M. Phys Status Solidi B. 2010; 247:1032–1038.
67. Balan A, Derlet PM, Rodriguez AF, Bansmann J, Yanes R, Nowak U, Kleibert A, Nolting F. Phys Rev Lett. 2014; 112:107201. [PubMed: 24679323]
68. Wells DM, Rossi G, Ferrando R, Palmer RE. Nanoscale. 2015; 7:6498–6503. [PubMed: 25660112]
69. Shelemin A, Kylián O, Hanuš J, Choukourov A, Melnichuk I, Serov A, Slavínská D, Biederman H. Vacuum. 2015; 120:162–169.
70. Podestà A, Borghi F, Indrieri M, Bovio S, Piazzoni C, Milani P. J Appl Phys. 2015; 118:234309.
71. Romer I, Wang ZW, Merrifield RC, Palmer RE, Lead J. Environ Sci Technol. 2016; 50:2183–2190. [PubMed: 26792384]
72. Della Foglia F, Chiarello GL, Dozzi MV, Piseri P, Bettini LG, Vinati S, Ducati C, Milani P, Selli E. Int J Hydrogen Energy. 2014; 39:13098–13104.
73. Ellis PR, Brown CM, Bishop PT, Yin J, Cooke K, Terry WD, Liu J, Yin F, Palmer RE. Faraday Discuss. 2016; 188:39–56. [PubMed: 27152749]
74. Spadaro MC, Luches P, Bertoni G, Grillo V, Turner S, Van Tendeloo G, Valeri S, D'Addato S. Nanotechnology. 2016; 27:425705. [PubMed: 27631569]
75. Mélinon P, Begin-Colin S, Duvail JL, Gauffre F, Boime NH, Ledoux G, Plain J, Reiss P, Silly F, Warot-Fonrose B. Phys Rep. 2014; 543:163–197.
76. Binns C, Qureshi M, Peddis D, Baker S, Howes P, Boatwright A, Cavill S, Deshi S, Lari L, Kröger R, Langridge S. Nano Lett. 2013; 13:3334–3339. [PubMed: 23746148]
77. D'Addato S, Pinotti D, Spadaro MC, Paolicelli G, Grillo V, Valeri S, Pasquali L, Bergamini L, Corni S. Beilstein J Nanotechnol. 2015; 6:404–413. [PubMed: 25821680]
78. Laskin J, Johnson GE, Prabhakaran V. J Phys Chem C. 2016; 120:23305–23322.
79. Blackmore CE, Rees NV, Palmer RE. Phys Chem Chem Phys. 2015; 17:28005–28009. [PubMed: 25776006]
80. Martinez L, Diaz M, Roman E, Ruano M, Llamosa PD, Huttel Y. Langmuir. 2012; 28:11241–11249. [PubMed: 22788661]
81. Benelmekki M, Bohra M, Kim JH, Diaz RE, Vernieres J, Grammatikopoulos P, Sowwan M. Nanoscale. 2014; 6:3532–3535. [PubMed: 24584692]
82. Llamosa D, Ruano M, Martinez L, Mayoral A, Roman E, Garcia-Hernandez M, Huttel Y. Nanoscale. 2014; 6:13483–13486. [PubMed: 25180699]
83. Johnson GE, Colby R, Laskin J. Nanoscale. 2015; 7:3491–3503. [PubMed: 25626391]
84. Johnson GE, Colby R, Engelhard M, Moon D, Laskin J. Nanoscale. 2015; 7:12379–12391. [PubMed: 26148814]
85. Benelmekki M, Vernieres J, Kim J-H, Diaz R-E, Grammatikopoulos P, Sowwan M. Mater Chem Phys. 2015; 151:275–281.
86. Singh V, Cassidy C, Abild-Pedersen F, Kim JH, Aranishi K, Kumar S, Lal C, Gspan C, Grogger W, Sowwan M. Nanoscale. 2015; 7:13387–13392. [PubMed: 26203627]

87. Grammatikopoulos P, Steinhauer S, Vernieres J, Singh V, Sowwan M. Adv Phys X. 2016; 1:81–100.

88. Grammatikopoulos P, Kioseoglou J, Galea A, Vernieres J, Benelmekki M, Diaz RE, Sowwan M. Nanoscale. 2016; 8:9780–9790. [PubMed: 27119383]

89. Mayoral A, Llamosa D, Huttel Y. Chem Commun. 2015; 51:8442–8445.

90. D'Addato S, Grillo V, Altieri S, Frabboni S, Valeri S. Appl Surf Sci. 2012; 260:13–16.

91. D'Addato S, Spadaro MC, Luches P, Grillo V, Frabboni S, Valeri S, Ferretti AM, Capetti E, Ponti A. Appl Surf Sci. 2014; 306:2–6.

92. NEXT-TIP. http://www.next-tip.com

93. Martinez L, Tello M, Diaz M, Roman E, Garcia R, Huttel Y. Rev Sci Instrum. 2011; 82:023710. [PubMed: 21361604]

94. Horcas I, Fernandez R, Gomez-Rodriguez JM, Colchero J, Gomez-Herrero J, Baro AM. Rev Sci Instrum. 2007; 78:013705. [PubMed: 17503926]

95. Garcia R, Losilla NS, Martínez J, Martinez RV, Palomares FJ, Huttel Y, Calvaresi M, Zerbetto F. Appl Phys Lett. 2010; 96:143110.

96. Redondo-Cubero A, Gago R, Palomares FJ, Mücklich A, Vinnichenko M, Vázquez L. Phys Rev B: Condens Matter. 2012; 86:085436.

97. Díaz M, Martínez L, Ruano MM, Llamosa D, Román PE, García-Hernandez M, Ballesteros C, Fermento R, Cebollada A, Armelles G, Huttel Y. J Nanopart Res. 2011; 13:5321–5333.

98. Mayoral A, Deepak FL, Esparza R, Casillas G, Magen C, Perez-Tijerina E, Jose-Yacaman M. Micron. 2012; 43:557–564.

99. Yan J, Wu G, Guan N, Li L, Li Z, Cao X. Phys Chem Chem Phys. 2013; 15:10978–10988. [PubMed: 23708180]

100. Shukla S, Seal S. Nanostruct Mater. 2000; 11:1181–1193.

101. Radnik, Jr, Mohr, C., Claus, P. Phys Chem Chem Phys. 2003; 5:172–177.

102. Peters S, Peredkov S, Neeb M, Eberhardt W, Al- Hada M. Surf Sci. 2013; 608:129–134.

103. Wertheim GK, DiCenzo SB. Phys Rev B: Condens Matter. 1988; 37:844–847. [PubMed: 9944577]

104. Villa A, Dimitratos N, Chan-Thaw CE, Hammond C, Veith GM, Wang D, Manzoli M, Prati L, Hutchings GJ. Chem Soc Rev. 2016; 45:4953–4994. [PubMed: 27200435]

105. Casaletto MP, Longo A, Martorana A, Prestianni A, Venezia AM. Surf Interface Anal. 2006; 38:215–218.

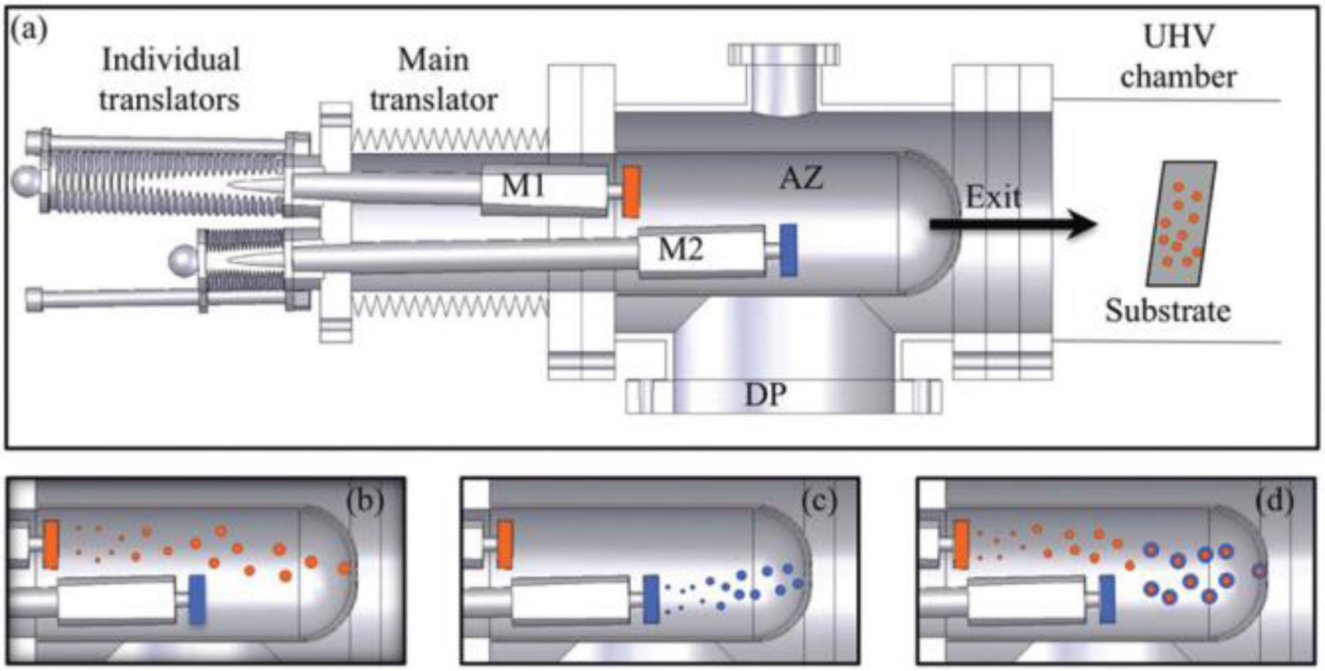

Fig. 1.

Schematic and principles of operation of MICS. (a) Two of the three magnetrons are presented as M1 and M2. These magnetrons are placed in the aggregation zone (AZ). (b) The growth of pure Au or (c) TiOx NPs was achieved using only one magnetron. (d) Growth of core@shell, Au@TiO_x by combining both magnetrons.

Europe PMC Funders Author Manuscripts

Europe PMC Funders Author Manuscripts

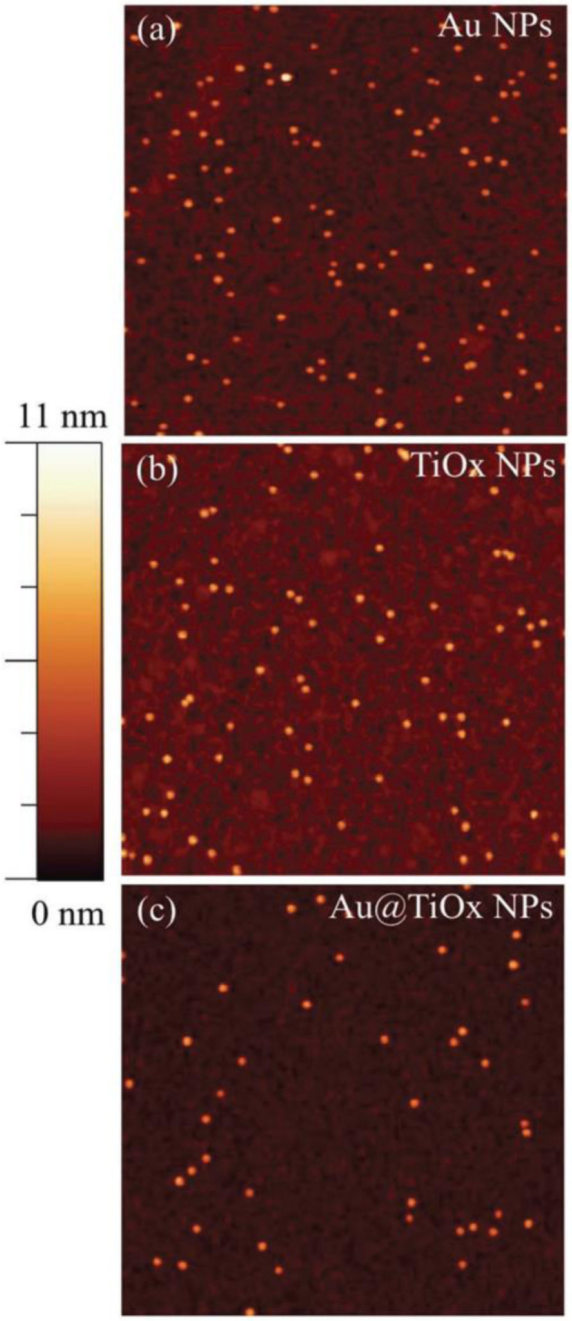

Fig. 2.

AFM characterization of the NPs deposits. (a) AFM images of pure Au NPs, (b) pure TiO_x NPs, and (c) core@shell, Au@TiO_x nanoparticles. All the figures are of 1 × 1 μm_2 size.

Europe PMC Funders Author Manuscripts

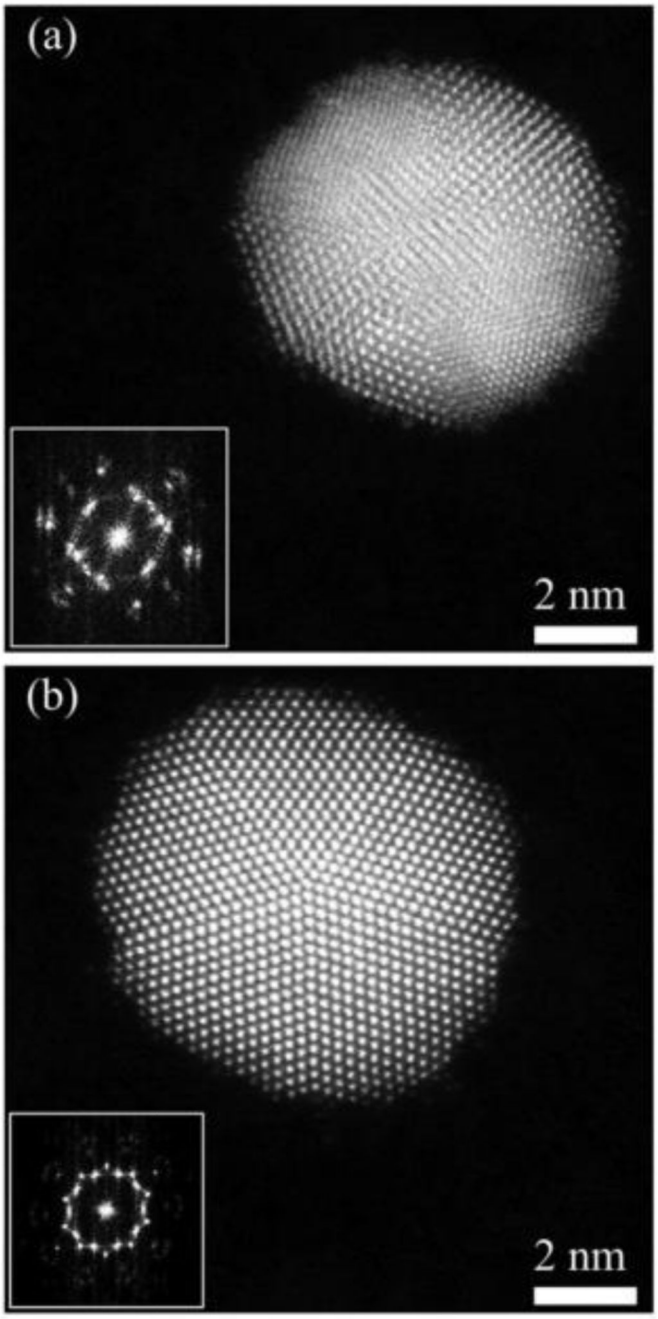

Fig. 3.

Atomic resolution Cs-corrected STEM characterization of Au nanoparticles. (a) Representative Au NP with an icosahedral structure and its corresponding fast Fourier transform (FFT) in the inset. (b) Representative Au NP with a decahedral structure and its corresponding FFT (inset).

Europe PMC Funders Author Manuscripts

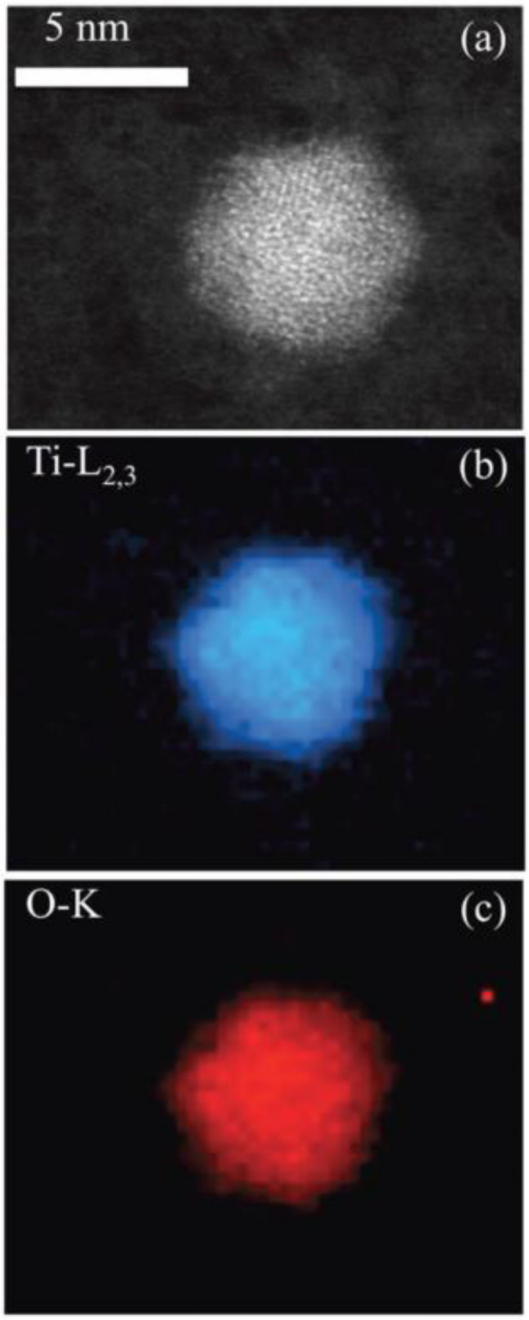

Fig. 4.

STEM characterization of TiO_x NPs nanoparticles. (a) Cscorrected STEM-HAADF image showing a poor crystalline order. (b) and (c) EELS maps at Ti $L_{2,3}$ and OK edges, respectively.

Europe PMC Funders Author Manuscripts

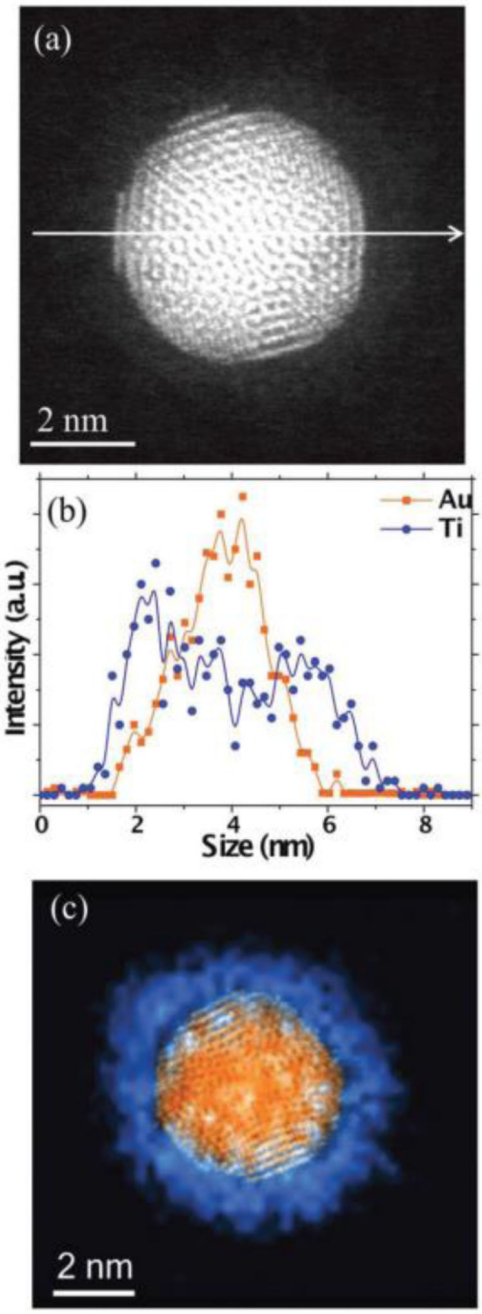

Fig. 5.

STEM characterization of the Au@TiO_x NPs nanoparticles. (a) Cscorrected STEM-HAADF image of Au@TiO_x Ih. (b) EDS intensity profiles extracted along the white arrow plotted in (a). (c) Cs-corrected STEM-HAADF image of an Au@TiO_x nanoparticle with the chemical mapping: Ti-$L_{2,3}$ signal (blue color) and the Au-$M_{5,4}$ signal (orange color).

Europe PMC Funders Author Manuscripts

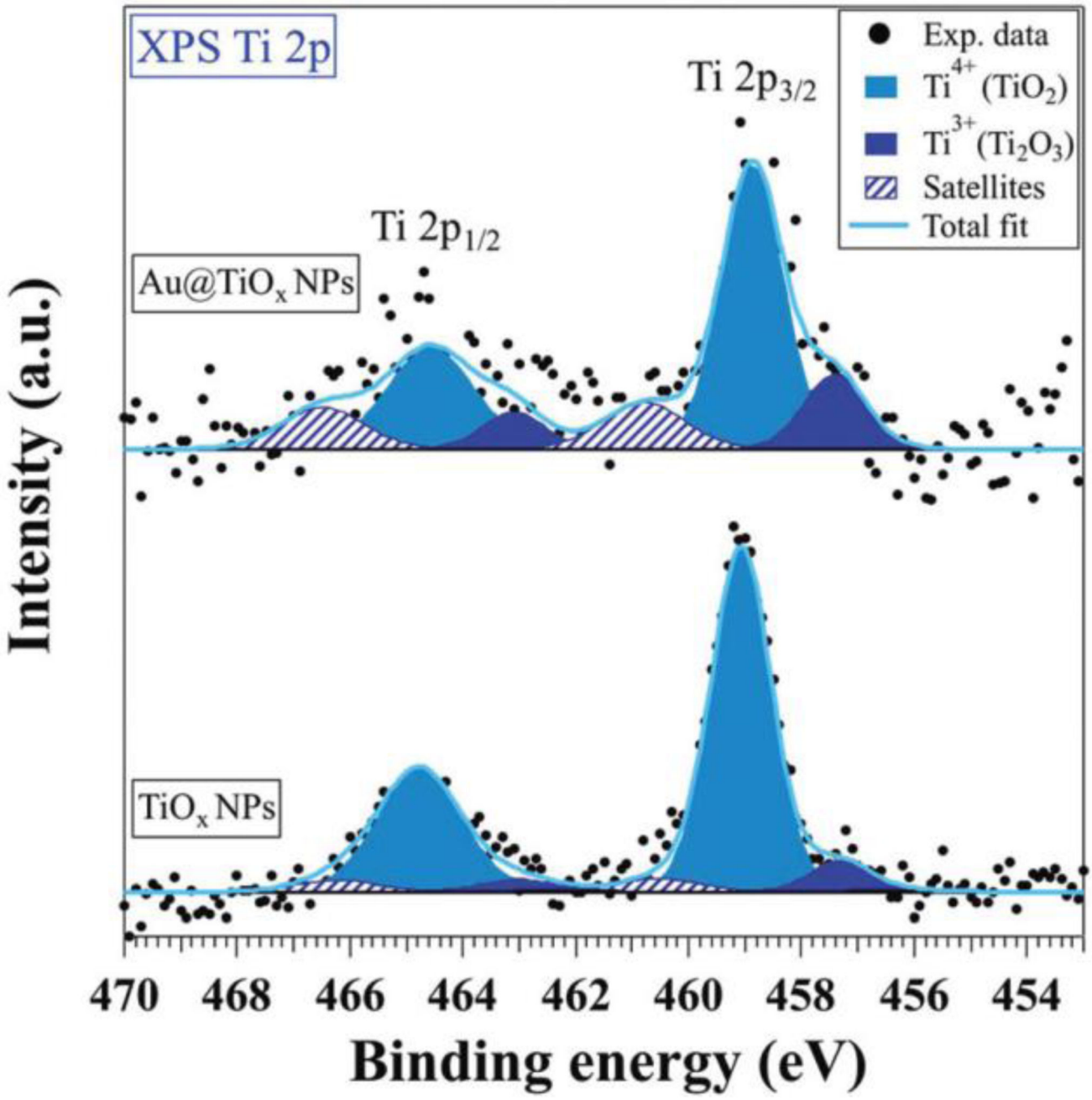

Fig. 6.
Electronic structure of TiO_x and Au@TiO_x NPs.

Europe PMC Funders Author Manuscripts

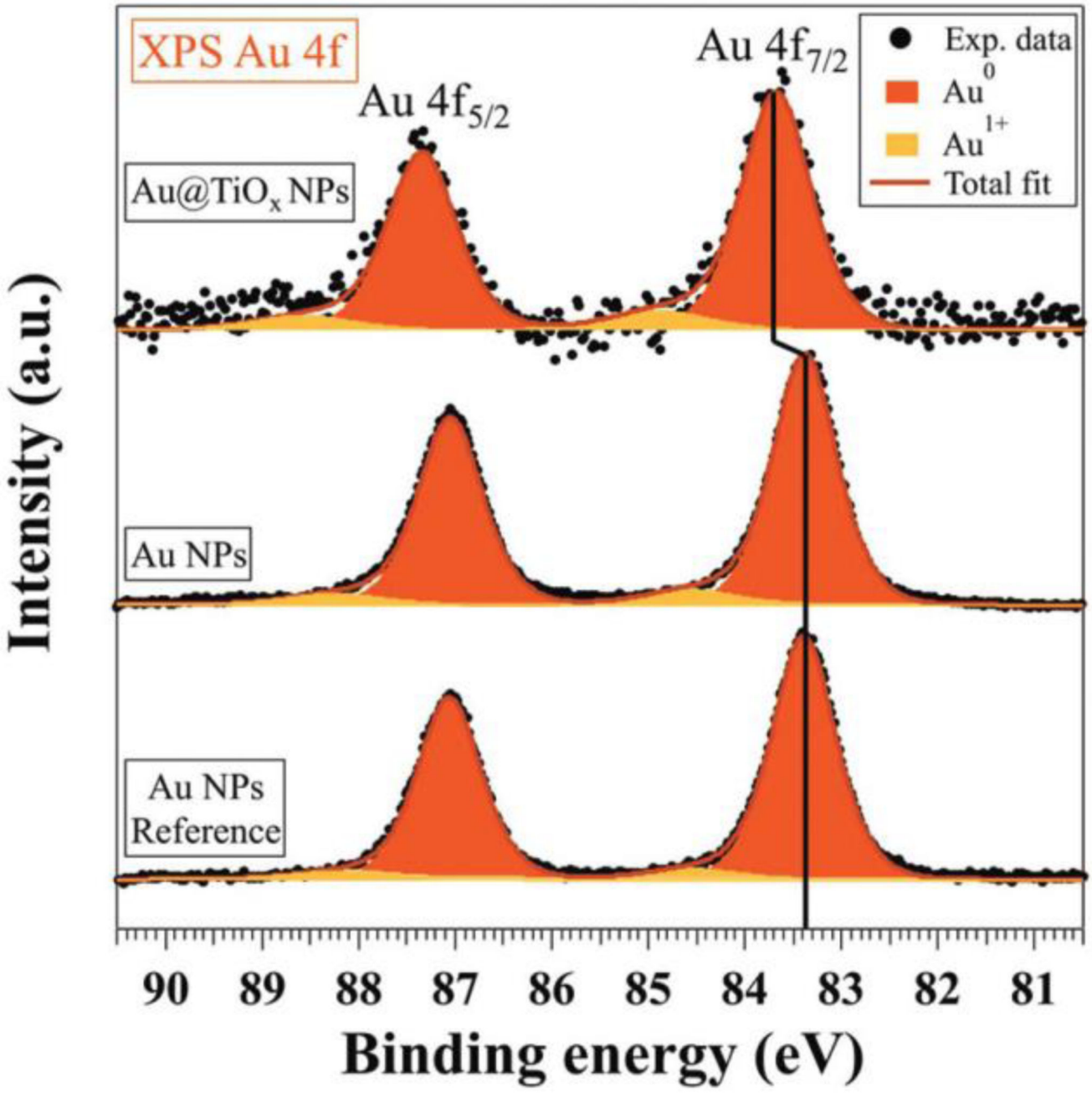

Fig. 7.
Electronic structure of Au and Au@TiO_x NPs.